Gruber, C., Gouweleeuw, B. (2019): Short-latency monitoring of continental, ocean- and atmospheric mass variations using GRACE intersatellite accelerations. - *Geophysical Journal International*, *217*, 1, pp. 714—728.

DOI: http://doi.org/10.1093/gji/ggz042

Geophysical Journal International

Geophys. J. Int. (2019) **217,** 714–728
Advance Access publication 2019 January 29
GJI Gravity, geodesy and tides

doi: 10.1093/gji/ggz042

Short-latency monitoring of continental, ocean- and atmospheric mass variations using GRACE intersatellite accelerations

Christian Gruber [1,2] and Ben Gouweleeuw[3]

[1] *Helmholtz Centre Potsdam, Research Center for Geosciences (GFZ), Section* 1.2*: Global Geomonitoring and Gravity Field, c/o DLR Oberpfaffenhofen, Münchener Strasse* 20, 82234 *Wessling, Germany*
[2] *Now at Trimble TerraSat, Haringstr. 19, 85635 Hoehenkirchen-Siegertsbrunn, Germany. E-mail: christian_gruber@trimble.com*
[3] *Helmholtz Centre Potsdam, Research Center for Geosciences (GFZ), Section* 5.4*: Hydrology, Telegrafenberg,* 14473 *Potsdam, Germany*

Accepted 2019 January 28. Received 2019 January 7; in original form 2017 December 28

SUMMARY

GRACE K-band intersatellite range observations have been processed in combination with precise orbit trajectories from reduced dynamic modelling and GNSS processing. These data have been inverted to mass equivalent quantities (water heights) by using physically motivated constraints in order to reduce well-known instabilities. In a first instance, the satellite observations are reduced using geophysical background modelling and implicitly continued downward using a rigorous formulation in terms of reproducing kernel functions which map time variable mass variations from Earth's fluid envelops to remotely sensed observations. The space-wise observation equations are well suited for a Kalman-filter measurement update approach which enables an enhanced temporal resolution of subweekly to daily time-series. For stochastic signal prediction and process model derivation, spatio-temporal correlations of mean hydrological and atmospheric signals have been used. It is shown that the GRACE dynamic measurements are converted to *in situ* observables, thus facilitating the combination with other data sources such as, for example higher resolution remote sensing data and/or available ground data. Through the consideration of full signal and measurement error covariances in a Kalman filter process, the effects of aliasing from poorly modelled or insufficiently available background information can be mitigated. We present the theoretical rational of the method, together with results for daily Kalman filtered solutions, for the full duration of the GRACE mission and numerical tests and comparisons to available operational GRACE products and inundation volumes. Finally, the major findings of these computations are listed.

Key words: Geopotential theory; Satellite geodesy; Satellite gravity; Time variable gravity.

1 INTRODUCTION

In recent decades, the determination and monitoring of Earth's time variable gravity field has significantly improved thanks to NASA/DLR's Gravity recovery and Climate Experiment (GRACE), Tapley *et al.* (2004). After 15 yr of satellite mission duration the detection and analysis of large scale continental surface- and groundwater storage changes, hitherto unknown precise deglaciation estimates over the polar regions, mega-thrust hazards induced by continental slips and earthquakes as well as viscoelastic uplift by postglacial isostatic adjustment (GIA) have been reported. Launched in 2002, the mission has ended 13 October 2017 long beyond its scheduled 5-yr life-time; new remotely sensed gravity observations are becoming available after the GRACE Follow-On mission launched May, 2018.

Up to now, data and analysis centers have been delivering several updated GRACE-based time-series of monthly mean gravity field products, which showed increased levels of agreement and promise for an anticipated pre-mission resolution capability of the twin satellite measurement principle over large geographic scales of several hundreds of kilometres.

Despite 15-yr worth of data, in-coherence between the gravity remote sensing results and 'ground truth' references persists, so that further refinements of data processing and analysis strategies remains a requirement. Some authors even refer to a 'quest for consistency', Van Camp *et al.* (2013) with regard to a comparison with ground observations, stemming from permanent GPS station networks, absolute gravimetry recordings and other mass transport or water volume related data (e.g. soil moisture, surface water runoff, river discharges).

Earth climate's natural variation and post-industrial intrusion of greenhouse gases has increased the need for a robust monitoring of the global water cycle. In this context, air and space-borne measurements are uniquely positioned to provide consistent and comprehensive data coverage for cryosphere- and hydrological studies, for example in, but not restricted to, remote areas subject to thawing

permafrost in the Arctic and polar regions, *cf*. Shabanloui & Müller (2015). Sophisticated methods need to be further refined for the retrieval of signals within short latencies and for the quantification of extreme events such as large floods, and severe droughts that can be deduced from periodical or permanent imprints to the Earth's gravity field.

One of the key variables for hydro-geological monitoring and modelling studies is the temporal variation of the water storage in groundwater aquifers. According to Güntner *et al.* (2006), assessing groundwater storage change is central to water management with regard to water resources, ecology (e.g. wetland preservation) or engineering (e.g. land subsidence due to groundwater withdrawal). Several studies have shown that groundwater depletion during droughts threatens future water security, for example in the Colorado river basin, *cf.* Castle *et al.* (2014), where GRACE revealed 65 km^3 groundwater depletion between 2004 and 2013. When combined with coincident data sets for snow water equivalent, GRACE observations have shown to be able to quantify surface water storage and soil water content changes within the global and regional water mass balance, with high accuracy (e.g. Famiglietti *et al.* 2011).

In the presented approach, residual daily mass equivalents of the atmosphere, non-steric ocean topography and gravity changes within the hydrological storage system are estimated in a Kalman filter approach from the observed acceleration differences between the GRACE twin satellites, known as acceleration approach, Rummel (1979). These extremely sensitive measurements, accurate to only a few tens of μGal are not only affected by irregularities of the gravity field (known as static gravity anomalies) but also from third body attractions (e.g. Sun, Moon and other planets), the Earth and Ocean dynamic responses (solid Earth tides, ocean tides), dissipative forces from Earth's albedo, solar radiation pressure variations and upper atmosphere particle friction. The latter forces were accurately registered by on-board accelerometry devices and enable their separation from the conservative forces. The accelerometry measurements are iteratively scaled and calibrated during a fit of precise dynamic space-craft trajectories to carrier phase observations from GPS high-low observations. After the scaling of empirical temperature induced accelerometer drifts acting on the accelerometer differences further nuisance parameters, such as KBR revolution specific calibration parameters, are co-estimated on a daily basis during the subsequent estimation process. Additionally, short-term atmospheric and non-steric ocean topography variations caused by weather-related phenomena with a duration length below the gravity field estimation period (daily/weekly/monthly) are removed beforehand.

The differential GRACE accelerations can be conveniently corrected for the listed effects that are acting on the twin satellites during orbital revolution. The remaining signal is then confined to continental hydrology, melting or accumulating ice sheets, non-steric seasonal water mass exchange, earthquakes and effects caused by glacial isostatic adjustment (GIA).

The relation of these residual observations with the time variable gravity field is solved on a spherical shell by a boundary value formulation wherein the influence of mass variations at the Earth's surface is weighted by it's distance to the observations between the twin satellites. In order to estimate the specific mass variation in discretized surface areas, a mathematical inverse formulation needs to be solved. Despite a large number of observation samples (every 5 s), the problem remains in practice ill-posed, due to an incomplete data coverage of the Earth's sphere in space and time (ground track coverage) and ambiguous signal continuation from orbital altitude downward to Earth's mean radius.

Therefore, it is useful to stabilize results using available geophysical background information for the expected signals and to model their stochastic behavior as an additional momentum. This can be done by using signal and error covariances in the time varying storage systems, as well as the noise characteristics of the (residual) observables from the remote sensor system. The latter noise type mainly stems from the ranging and accelerometer instruments, the orbital trajectory determination and the subtracted background model uncertainty.

For the transformation into proxy observables that can be directly mapped to the gravity field, we need to introduce the forces perpendicular to the line-of-sight between the twin space-crafts. For this purpose, the equations of motion for the satellite trajectories are used to supply additional information in the direction perpendicular to the intersatellite ranging. Specifically, the observed KBR intersatellite accelerations miss either a constant (zero-frequency) of the even-degree spherical harmonics when orbiting strictly in latitude direction or cannot sense zero order (zonal) spherical harmonics when orbiting in the longitude direction or a combination of both for the general case. This explains why KBR-only measurements in practice are rank deficient and cannot determine an orthonormal functional space without further information.

For this purpose we complement the ranging data by the velocities obtained from reduced dynamic precise orbit determination. We admit the re-introduction of the background force model from the orbit integration into the solution. In our approach, the time variable result from the previous day is used in addition to the background force model. Therefore, the perpendicular acceleration in eq. (B8) is biased to the time-variable gravity field of the previous day. Since the measurement update in the Kalman filter is a weighted combination between previous day and current observation data, we believe that this is maintainable and results, as with Kalman filtering, in a time-lag. Clearly, for an effective surface resolution below $3^\circ \times 3^\circ$ (i.e. spherical harmonic degree/order $\leq$60), sampling over the past 4 d with *ca*. 16 revolutions per day is required. The perpendicular forcing in eq. (B8), delayed by 1 d, does not severely affect the filtered estimates in this context.

Switching to Kalman smoothing (forward and backward filtering) in post processing then entirely revises this lag. The goal for this project was, however, a near-real-time scenario. In the current setting a latency of 2−3 d was achieved that can be shortened in the future down to just 1 d. For alternative acceleration-based solutions and further discussion on the matter, the reader is referred to, for example Chen *et al.* (2015) and Weigelt (2017).

2 FUNDAMENTALS

The use of multipole techniques, that is estimation of spherical harmonic coefficients (Hobson 1955), has become a standard approach to GRACE data processing. However, a uniform sample coverage on the sphere can generally not be fulfilled by low Earth orbiting (LEO) satellites without a non-conservative force compensation that would preserve the orbital altitude.

The satellite ground tracks then strongly vary during orbital decay and the spherical sampling is not well-balanced spatially due to non-repeat cycle orbits for specific evaluation time-spans, or unforeseen data gaps caused by satellite maneuvers, resulting in an alternating number of sample observations in each month. This

dynamically changing configuration of the observation system between subsequent months affects the coefficient estimation which makes it difficult, if not impossible, to interpret the results on short timescales, for example from 1 month to the following.

Anisotropic artefacts, typically visible as stripings in the north-south direction in the GRACE derived gravity field solutions, are a well-known phenomena. To this end, extensive efforts have been made since the beginning of the GRACE mission concerning post-filtering of the unconstrained GRACE L2 data-products, for instance Swenson & Wahr (2006), Kusche *et al.* (2009), Klees *et al.* (2008), Zhang *et al.* (2009), applying methods of destriping and/or smoothing. In Schmeer *et al.* (2012), the mass signal is filtered by means of empirical orthogonal functions in order to attribute the signal to mass transfer within the continental hydrosphere on subseasonal to seasonal timescales.

In recent years, increasingly more attention is payed to a physically motivated stabilization of the estimates by appropriate constraining. Such constraints can be constructed in the spatial domain in analogy to Gaussian smoothing as well as in the frequency domain (e.g. Rowlands *et al.* 2010; Lemoine *et al.* 2013).

Our daily gravity field solutions have been computed by means of spherical radial basis functions (RBFs) that are localized in space and frequency domain. It is well known that an optimal localization in both square integrable domains is not possible (*cf.* Landau 1985; Schneider 1997). In this formulation, the gravitational potential of a surface layer on the reference sphere, with the radius equal to the semi-major axis of the Earth's ellipsoid, to an arbitrary point in external space can be modelled. The relation between this layer and the gravitational potential observations from artificial satellite systems are provided by Poisson's integral. For a brief introduction, the reader is referred to Appendix A.

Poisson's kernel function provides the topologically compact spatial counterpart to spherical harmonic coefficient estimation by the solution of the corresponding surface integrals, but with implicit weights reflecting the spherical distance between observation and surface points. In combination with the remove-compute-restore principle of physical geodesy, regional evaluations can be computed, assuming the spatial correlation half-lengths of the time variable mass signals are relatively small, and the contribution of the laterally distant masses (far zone) to become negligible.

The derivation of a tailored kernel for the application of Poisson's integral to the GRACE observables was shown by Novák (2007) based on range-accelerations. For more details, the reader is referred to Appendix B. In Gruber *et al.* (2013), the taylored kernel has been used in a case study with Kalman filtering to derive daily gravity maps from GRACE.

Reducing the surface gravity V by a static background model, V_{EGM}, leaves the remaining signal attributed to the time-variable gravitational potential, δT. Applying Brun's formula then leads to height variations or undulations of the geoid, δN, with respect to the equi-potential surface of the Earth's gravitational field that coincides with the equilibrium figure of mean sea surface

$$\delta N = \delta T \,/\gamma, \tag{1}$$

where $\gamma = \mathrm{grad}\, U$ is the normal gravity. The time-variable potential is composed of Laplace surface harmonics

$$\delta T = \sum_n \delta T_n \,, \tag{2}$$

per degree n, given by

$$\delta T_n = \frac{2n+1}{4\pi} \int_\omega (V - V_{\mathrm{EGM}}) \left(\frac{\mathrm{R}}{r}\right)^{n+1} P_n(\cos\psi)\, \mathrm{d}\omega \,, \tag{3}$$

where R is the mean radius of the Earth and r the radius to the remote observation, P_n are Legendre polynomials and ψ is the spherical distance between surface gravity values and observation points. $\int_\omega \mathrm{d}\omega$ is the integration over the sphere ($\omega = \{\mathbf{y} |\, y_1^2 + y_2^2 + y_3^2 = \mathrm{R}\}$) with $\mathrm{d}\omega = \sin\theta \mathrm{d}\theta \mathrm{d}\lambda$ and θ and λ are the geocentric colatitude and longitude. The geoid height variations, eq. (1), can be further computed as equivalent layer thickness, δh of surface water mass if an elastic deformation of the Earth is taken into account, *cf.* Wahr *et al.* (1998) and in analogy with eq. (2)

$$\delta h = \frac{\rho_e}{3\rho_w} \sum_n \frac{2n+1}{1+k_n}\, \delta N_n \,, \tag{4}$$

with load Love numbers k_n according to Farrell (1972), which characterize the deformation of the elastic Earth, an average density of $\rho_e = 5517\,\mathrm{kg\,m^{-3}}$ and a specific density of water $\rho_w = 1000\,\mathrm{kg\,m^{-3}}$.

The GRACE gradient kernel $\mathcal{H}$, see Appendix B, eq. (B11) integrates geo-potential signal from Earth' surface mass contrast into proxy observables at satellite altitude. Similarly, we can put for proxy observations, eq. (B6)

$$\ell = \frac{1}{4\pi} \int_\omega f(\mathcal{H})\, \delta h \, \mathrm{d}\omega \,, \tag{5}$$

such that estimates for the equivalent layer thickness in the gridpoints are found by least-squares inversion. Their stochastic behavior can be investigated (from trajectories) by empirical variances

$$\sigma_s^2(\delta h) = \mathrm{diag}\left(H^T C_\ell^{-1} H\right)^{-1} \,, \tag{6}$$

where $H = f(\mathcal{H})_{[\mathrm{u}\times\mathrm{s}]}$ is the linear relation between surface gridpoints of dimension $[1 \times s]$ and an observation vector of dimension $[u \times 1]$, connected in each observable by the gradient kernel, $\mathcal{H}$ and a function of conversion, eq. (4). The surface grid vector is defined by the density of the integration grid (see next section). The observables follow the GRACE sampling rate (5 s) and sequence. The error covariance estimates, C_ℓ are found from average autocorrelations of the observation error ε_ℓ, *cf.* chapter 5The empirical variances from eq. (6) were approximated in the sequence of this study by a facile latitude dependent relation

$$\sigma_s^2 = 50\mathrm{mm}^2 \sqrt[20]{\sin\theta_s} \,, \qquad 0 < \theta_s < \pi \,, \tag{7}$$

resulting for the equator in *ca.* 7 mm. They have been added to the process error covariance modelling that is derived from a globally approximated, homogeneous and isotropic averaging operator and therefore with equal variance and correlation throughout all gridpoints.

3 REMARKS ON THE INTEGRATION GRID

The integration requires a regular surface grid. Considering an equiangular grid, surface elements are infinitely narrowing towards the poles which implies higher spatial resolution than in lower latitudes. As the satellite data sampling (ground track density) substantially increases with latitude, the redundancy between observation equations and partial derivatives in the gridpoints vary, correspongingly.

Since the Poisson kernel has a singularity at the 'north pole' and is regular in all other points in space, computations need to be based

on center grid cell values rather than corner values. We have fixed the integration grid to equal area surface tiles, thereby substantially reducing the number of processed grid tiles in comparison to the equi-angular integration grid: $2^\circ \times 2^\circ$ equal area mean values equal $\sim 10^4$, and correspond to a spherical harmonic resolution of degree and order 90. A substantual performance gain is achieved, since otherwise the equivalent of 16 200 grid cells is required to integrate an equi-angular grid.

As a consequence of the above mentioned sampling, higher latitudes now reflect higher confidences (i.e. lower formal root mean square errors) than equatorial latitudes and have to be taken into account by eqs (6) and (7).

4 LEAST SQUARES PREDICTION AND REGULARIZATION

For the first step in the Kalman filtering, we follow Kurtenbach *et al.* (2012) by propagating equivalent water heights and error covariances by least-squares prediction. Moritz (1980) and Krarup (2006) have shown that the predicted undulations are found by

$$\delta\widetilde{h}_P = \sum_{i=1}^{s}\sum_{k=1}^{s} C_{P_k} C_{ik}^{-1} \delta h_i \ , \tag{8}$$

where

C_{P_k} : cross − correlations between predicted and orig. points
C_{ik} : auto − correlations in the orig. points,

and s is the number of gridpoints. We therefore need to derive auto- and cross-covariance functions in the surface gridpoints from available external (empirical) data sets. The predicted values after a time-step Δt become

$$\delta\widetilde{h}_t = B_{\Delta t}\delta h_{t-\Delta t} + w \ , \quad E[w] = 0 \tag{9}$$

and the corresponding error covariances are predicted by

$$\widetilde{\Sigma}_{\delta h} = B_{\Delta t}\Sigma_{\delta h} B_{\Delta t}^T \ , \tag{10}$$

thereby using the error estimates from the previous Kalman update and the least-squares prediction matrix

$$B_{\Delta t} = C_{t,t-\Delta t} C_n^{-1} \ . \tag{11}$$

The covariances, C_n, for the surface areas enter in this context as the sum of empirical error variances for the surface grid values (eq. 7),

$$C_s = \begin{cases} \mathrm{diag}(C_s) = & \sigma_s^2 \\ 0 & \text{otherwise} \end{cases} \ , \tag{12}$$

and external process auto-covariances of the time-variable signal estimates at timestep $t - \Delta t$,

$$C_n = C_s + C_{t-\Delta t} \ . \tag{13}$$

The process cross-covariances then relate the grid values in $\mathbf{y} = \{\theta, \lambda, \mathrm{R}\}$ from the current time-step with the previous

$$C_{t,t-\Delta t} \equiv \mathrm{M}[f(\mathbf{y}_t) f(\mathbf{y}_{t-\Delta t})] \ , \tag{14}$$

by the averaging operator M. The results are obtained by computing the spatial averages of the cross covariances between subsequent daily hydrological, non-tidal ocean- and atmospheric mass variations and GRACE derived surface mass estimates. The average signal auto-covariances at time-step t are obtained correspondingly,

$$C_t \equiv \mathrm{M}[f(\mathbf{y}_t) f(\mathbf{y}_t)] \ . \tag{15}$$

Thus far, posteriori error covariances after least-squares signal prediction are found from the expected value covariances in t, with $C_t \approx E_t$, and predicted values from application of the prediction matrix, eq. (11) to the cross-covariances

$$Q_t = C_t - B_{\Delta t}\, C_{t-\Delta t,t} \ . \tag{16}$$

Both the prediction matrix $B_{\Delta t}$ and the prediction error covariances Q_t define the Kalman process model and are applied to the filtering before the measurement update in each consecutive processing step.

Three types of signals dominate the time variable gravity changes in this respect. First, the short-term atmospheric and non-tidal ocean mass variations, mainly caused by water evaporation and non-steric sea surface topography. These are regularly published alongside the monthly gravity field products and stem from external data sources such as surface pressure records from the European Centre for Medium-Range Weather Forecasts (ECMWF) and the Ocean Model for Circulation and Tides (OMCT), Dobslaw *et al.* (2013). They are provided in an external operational product, AOD1B, and are the strongest aliasing signal due to their high variability that is below the feasible GRACE temporal solution.

In the current processing, 6 hourly files were removed from the GRACE gradient differences beforehand and were averaged into daily products used for the empirical auto- and cross-covariance estimates. We propagate their characteristics as background model deficiency, approximated by 1/3 of the AOD1B signal, through the Kalman filter, that is process error prediction and transition.

Secondly, the Water Gap Hydrological Model (WGHM, Döll *et al.* 2003) was used to derive the signal covariances for continental hydrology. To achieve sufficient time-averaging, we stacked the external data set, that is same calendar month were averaged over the time-span of 15 yr.

Thirdly, with 15 yr of GRACE data being analysed at GFZ, we used GRACE RL5a solutions, Dahle *et al.* (2012) based on the same data pre-processing, in order to derive signal covariances, which are used in addition to compensate for missing information in the process model, such as, for example glacial isostatic adjustment (GIA) and earthquakes. The monthly time-step was hereby downscaled to a daily step.

In Kurtenbach *et al.* (2012), and more recently, Kvas *et al.* (2016), similar external data have been successfully applied for process model derivation and usage in a Kalman smoother. Tangdamrongsub *et al.* (2012) fitted a noise function of exponential decay to external hydrology to obtain smooth empirical functions for the space and time covariances.

A proper estimation of the covariance function in the Kalman prediction step requires a statistical distribution (stationary regime) with a small variance. It is pointed out that stochastic prediction can be applied only to the stationary signal. Therefore, a bias and a secular trend as well as the seasonal signal are removed from the surface grid cells in every prediction step. Fig. 1 outlines the reduction step in terms of variations with respect to the equi-potential surface coinciding with mean sea level. For the Ocean Surface, the secular trend and seasonal mass variability is assumed to be homogeneously distributed (eustasy). After predicting new values, the secular trends, biases and seasonal signals are added back to the results again.

To obtain continuous covariance functions, we applied an approximation by a sequence of Tchebyshev polynomials with limited bandwidth after the estimation of auto- and cross-covariances from the discrete averaging operator M, in eqs (14 and 15). In Fig. 2 the signal covariance function estimates for the external data products are depicted. Since the AOD1B and hydrology signals together exceed the strength of the available GRACE results, we

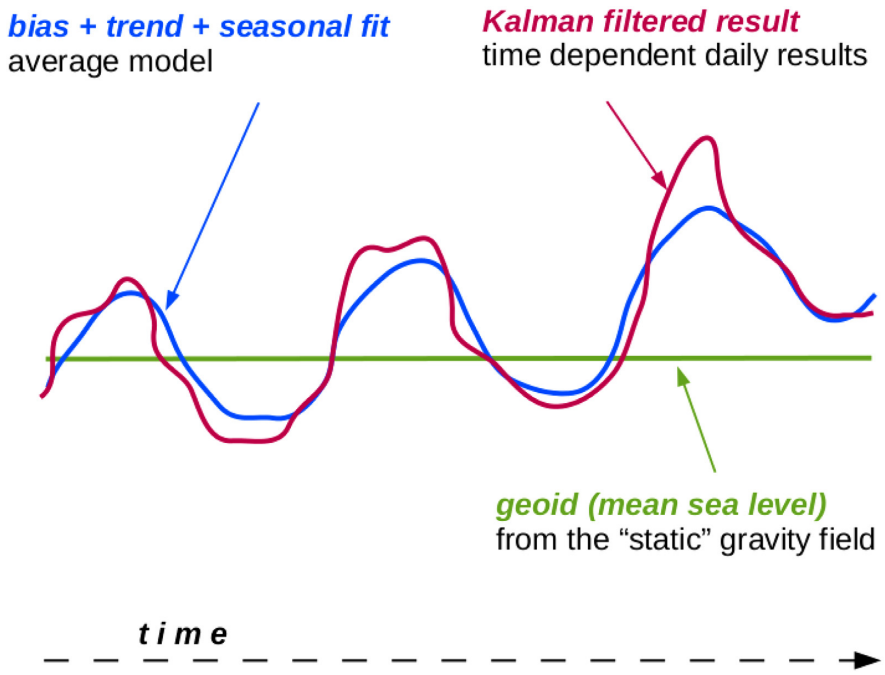

Figure 1. Illustration of the added value from a Kalman filtered solutions and the reduced average model.

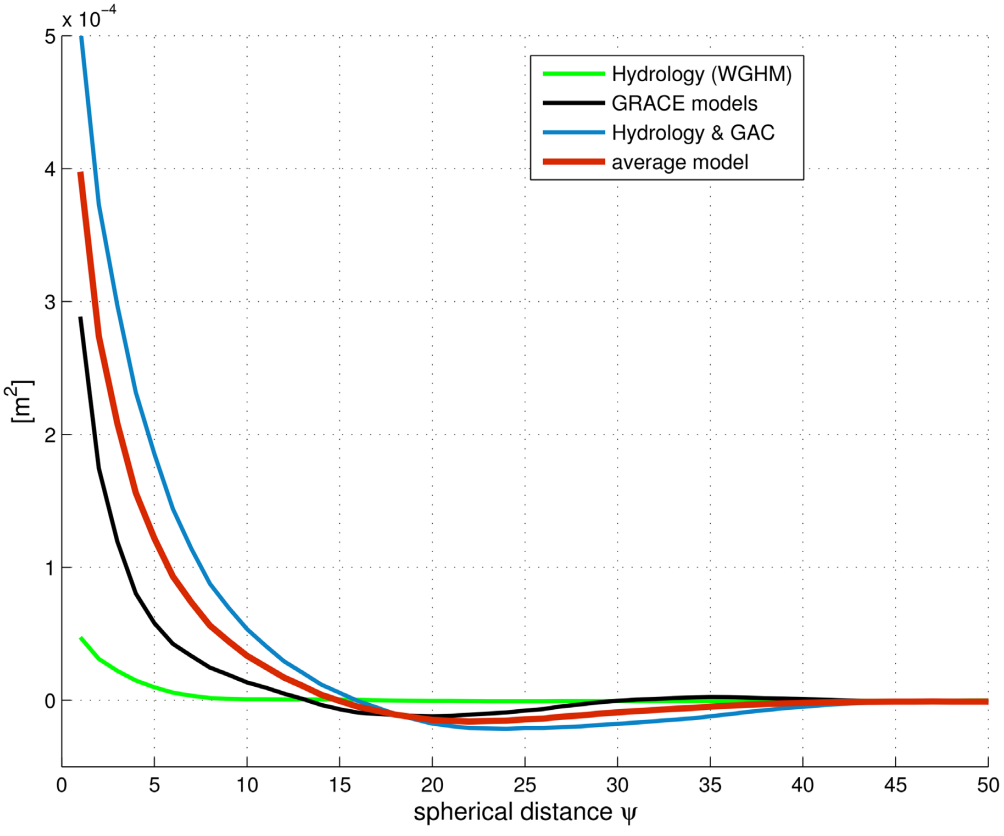

Figure 2. Empirical covariance functions for the temporal prediction step. The GRACE L2 and hydrological data concern the residual signal after removal of an average model, the AOD1B (GAC) signal has been used to 30 per cent of it's full signal strength.

combined them to produce the average of both. The continuous covariance function estimates are then isotropically distributed in a Toeplitz-matrix scheme, and to result in a positive definite matrix, the empirical signal variances (eq. 7) have been added.

To restrict the corresponding application domains for the derived covariance functions, three kinds of additional decorrelation masks for the surface tiles were effectively applied in order to further refine the filtering in the Kalman process. First, a domain mask L that sets

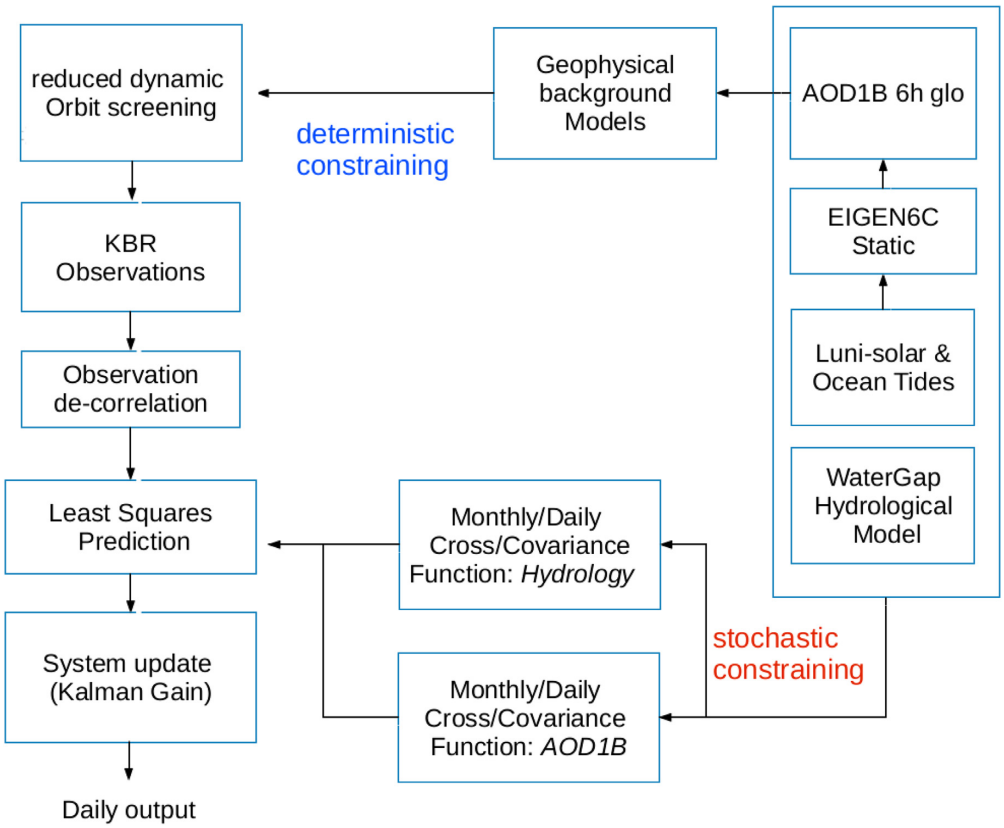

Figure 3. Applied processing scheme for short-latency mass variations. Geophysical background knowledge is introduced for observation reduction while the corresponding stochastic properties are entering the system filter.

the error covariances for continental hydrology estimates over the oceans to zero,

$$\mathrm{L} = l\,l^{\mathrm{T}}, \quad \text{with } l = \begin{cases} 1 & \text{overland} \\ 0 & \text{else} \end{cases}. \tag{17}$$

Secondly, a spatial damping for the GRACE derived covariances of the type

$$\Xi = (1 + \cos\psi_{ij})/2\,, \tag{18}$$

where ψ_{ij} are the spherical distances between the grid cells, see eq. (B18). Thirdly, a latitude dependent mask according to atmospheric cirulcation in the tropical convergence zone,

$$\vartheta_{\mathrm{I}} = \begin{cases} 1\ \forall\ -30^\circ < \phi < 30^\circ & \text{tropical zone} \\ 0 & \text{otherwise} \end{cases}$$

and the remainder

$$\vartheta_{\mathrm{II}} = \begin{cases} 1\ \forall\ |\phi| \geqslant 30^\circ & \text{polar and mid} - \text{latitude zone} \\ 0 & \text{otherwise} \end{cases},$$

that results in

$$\Theta = \vartheta_{\mathrm{I}}\,\vartheta_{\mathrm{I}}^{\mathrm{T}} + \vartheta_{\mathrm{II}}\,\vartheta_{\mathrm{II}}^{\mathrm{T}}\,, \tag{19}$$

decorrelating thus the tropical zone from the remaining latitudes.

5 THE KALMAN FILTER APPLIED TO GLOBAL DATA GRIDS

The feasibility of daily Kalman solutions for GRACE data was first demonstrated in Kurtenbach *et al.* (2009), which presents daily estimates for the solution of the first boundary-value problem in physical geodesy by means of spherical harmonic coefficient estimates. Using the GRACE gradient kernel, eq. (B11) a solution in each grid cell is computed accordingly.

The benefit of the Kalman filter over a rigorous least-squares inversion is that it provides additional information to the system based on assumed knowledge of how the states (here: mass variations) evolve in time. Instead of minimizing the least squares observation errors the trace of the *a posteriori* covariances is minimized (*cf.* Bierman 1977).

According to Petrovello (2013), the Kalman filter therefore typically provides temporally smoother and more accurate solutions if the assumptions regarding the evolution of the states are correct. Moreover, outliers are identifiable and can be discarded from processing during this step.

The use of a Kalman filter results in short latencies with respect to the observed signal, since no data accumulation is necessary, weighting the previous state with the new observations. As aliasing issues are mitigated, local resolvability is confined to the vicinity of ground track availability. Fine-resolution models are thus limited by flyover events in combination with background knowledge. For longer time-spans and denser sampling, however, it will lead to more averaging of the causing events, and therefore a damping effect. While the trade-off between spatial coverage and temporal resolution can be optimized in the Kalman filter, damping of the signal remains inevitable.

The *a priori* states are predicted using the most recent estimate for the state vector. The state transition is based on a deterministic model forecasting the mean time evolution of the data. This deterministic model stems from a fitted bias and secular trend as well as the seasonal component. In absence of the rigorous physical

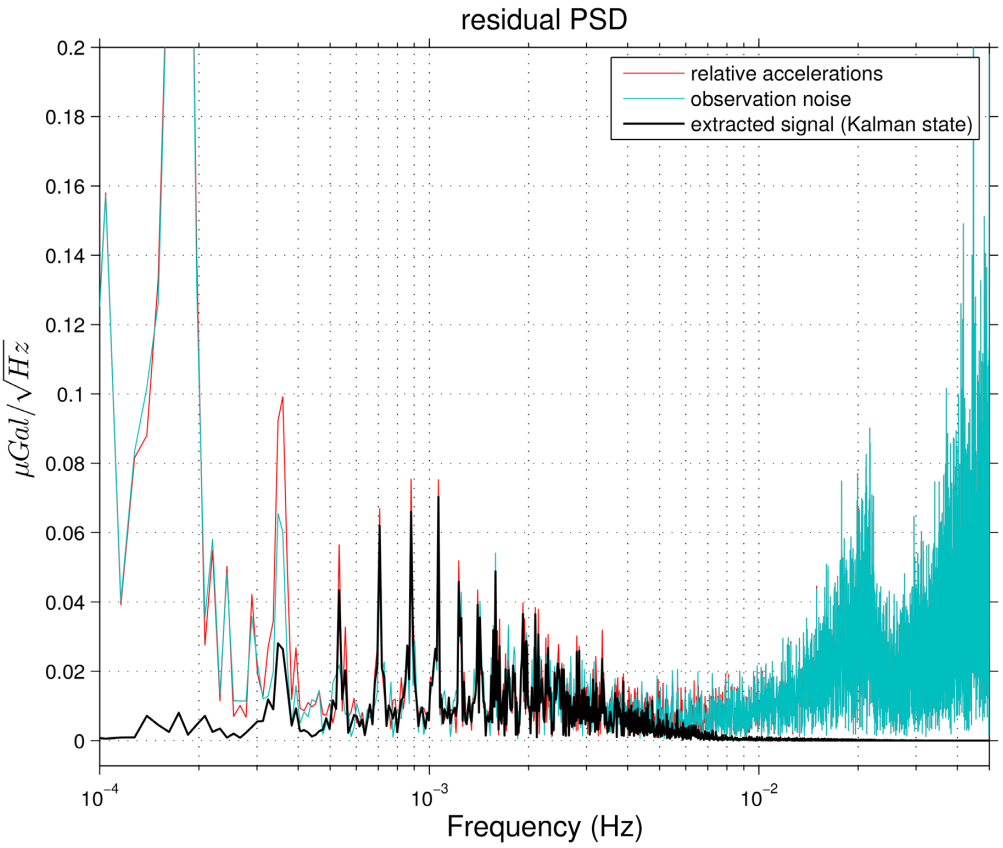

Figure 4. Power spectral densities of GRACE relative accelerations in line of sight, the extracted signal (Kalman state) and the residual observation noise.

Table 1. Applied geophysical model reductions during data preprocessing.

Ocean tides, EOT 11a, degree/order 120, Savcenko & Bosch (2011)
Direct planetary and Earth tides, IERS Conventions (2010)
Petit & Luzum (2010)
Atmospheric and non-tidal Oceanic de-aliasing, AOD1B RL5
Calibrated GRACE accelerometry data
Static gravity field, EIGEN_6C up to degree/order 150
Time variable gravity field, EIGEN_6C up to degree/order 50

knowledge of the system, our state transition is further completed by stochastic prediction, where the propagation from 1 d to the next follows least-squares prediction. The estimates for the time correlations, that is process cross-correlations, are derived from available GRACE solutions, hydrological data and the corresponding atmospheric and non-steric ocean variability (Section 4).

Fig. 3 shows a scheme for the applied filtering. Background modelling enters the solutions as deterministic constraint (remove-restore) and the Var/Covariance modelling as stochastic constraining. Daily system update after computing the Kalman gain results in the output grids.

The covariance update after the prediction in eq. (10) thus becomes

$$\widehat{\Sigma}_{\delta h} = \widetilde{\Sigma}_{\delta h} + \mathrm{L} \circ Q_k^{\mathrm{HYD}} + \Theta \circ Q_k^{\mathrm{GAC}} + \Xi \circ Q_k^{\mathrm{GRACE}} , \tag{20}$$

where the masks (L, Θ and Ξ) are applied as element-wise (Hadamard) products. This type of spatial allocation for the respective covariance domains is an asset over signal processing in spectral domain where covariance propagation becomes necessary (e.g. Rowlands *et al.* 2010).

The observation residuals for the measurement updates in each kth-step are obtained after the time-update (chapter 3), by

$$\ell'_k = \ell_k - H_k \delta\widetilde{h}_k, \quad \ell' \sim \mathcal{N}(0, R) \tag{21}$$

with estimates for the error covariances of the residuals,

$$R_{k,k-\tau} = \mathrm{E}\left[(\ell'_k - \mu)(\ell'_{k-\tau} - \mu)\right]/\sigma^2_{\ell}, \tag{22}$$

where τ is the time lag of the data sampling, μ is the average value and E is the expected value. It should be pointed out that the effective signal from the surface grid values δh in eq. (21) is very small,

$$\frac{|H\delta h|}{|\ell|} \ll 1 , \tag{23}$$

such that $\ell' \approx \ell$ can serve as a good initial estimate for the observation error covariances. In order to make the sample covariances representative over time, the daily observation covariances are combined as moving averages with previous estimates. The effective observation decorrelation (whitening) is then applied over a correlation length below 2 orbital revolutions (*ca*. 3 hr), corresponding to a filter bandwidth of ≈0.1–100 mHz.

Together with the Kalman gain function

$$K_k = \widehat{\Sigma}_k H_k^{\mathrm{T}} (H_k \widehat{\Sigma}_k H_k^{\mathrm{T}} + R_k)^{-1} , \tag{24}$$

the measurement update is computed

$$\delta h_k = \delta\widetilde{h}_k + K_k \cdot \ell'_k . \tag{25}$$

At this point the error covariance estimates from eq. (22) are once re-iterated by introducing the result from eq. (25) into eq. (21). Fig. 4 shows the obtained signal estimates for the Kalman states, the

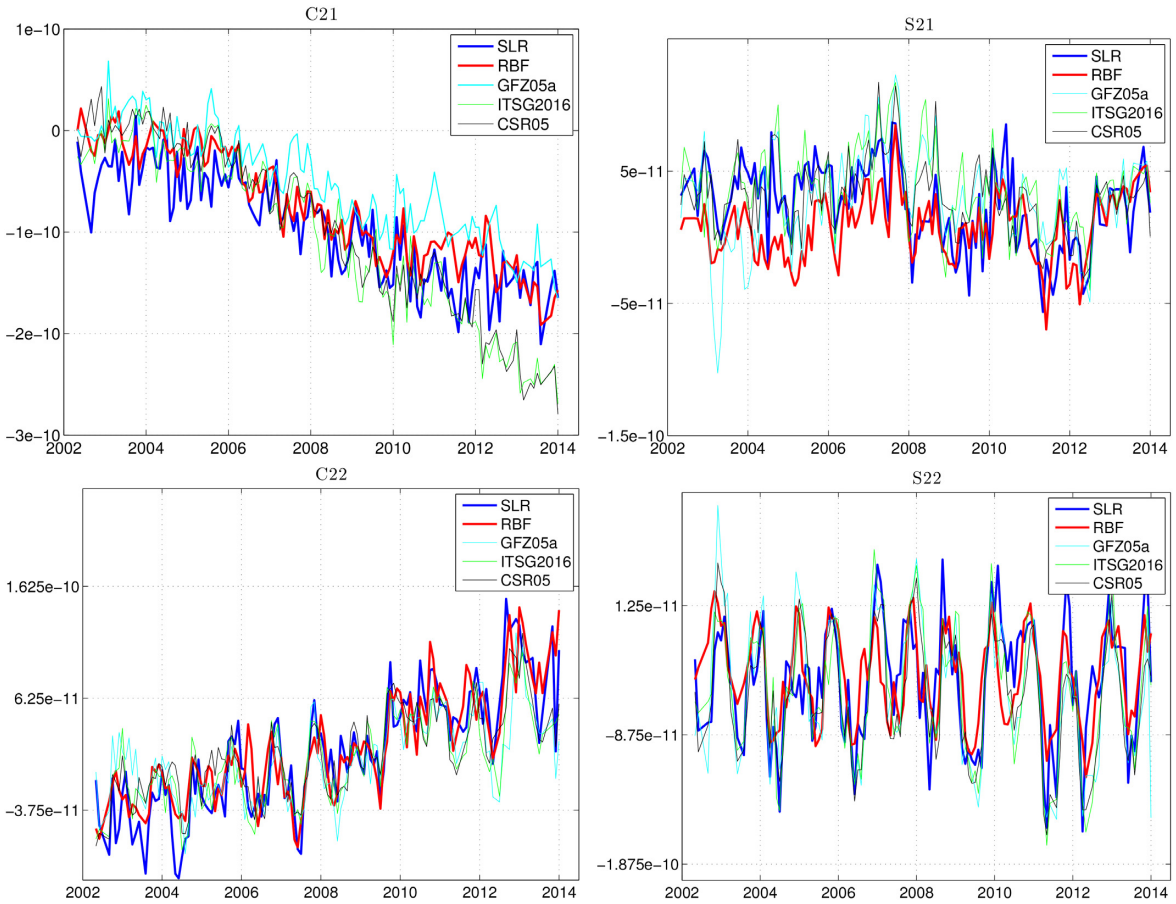

Figure 5. Time-series for ΔC_{21}, ΔS_{21}, ΔC_{22}, ΔS_{22} in agreement to SLR solutions. GFZ RBF solutions have been monthly averaged to comply with the sampling of the other data sets.

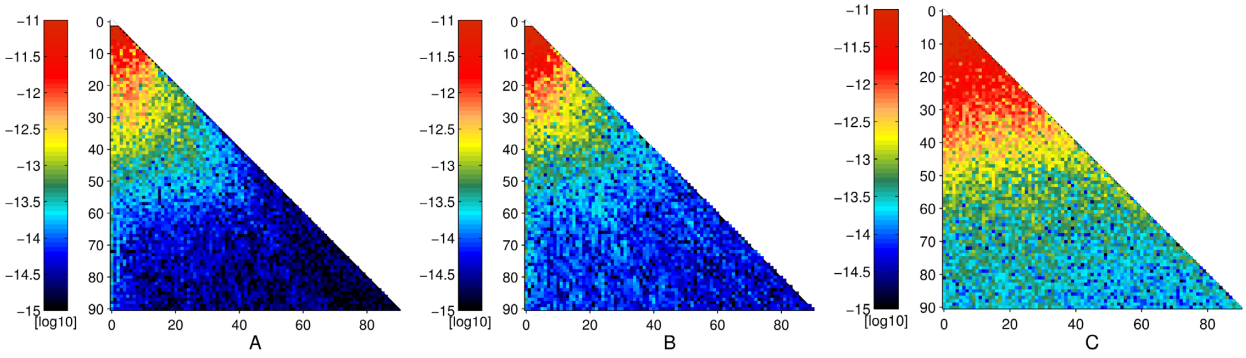

Figure 6. (A) The spherical harmonic amplitudes for the daily Kalman contribution, that is prediction and update, (B) Kalman state w.r.t the average time-variable background and (C) the full signal after restore with the subtracted average model. Units in [m] EWH.

GRACE acceleration differences containing the time-variable gravity signal and the observation residuals after the Kalman filtering. As expected, higher frequencies are predominantly contaminated by noise, stemming from the 2nd-order differentiation. Covariance propagation eventually completes the Kalman update,

$$\Sigma_k = (I - K_k H_k)\widehat{\Sigma}_k \,, \tag{26}$$

with the identity matrix I and finalizes the error propagation for the respective day.

6 PREPROCESSING OF THE DATA

For the orbit and force models in this study, the GFZ orbit integration software EPOS-OC was used, based on precise GPS network and LEO computation algorithms. Main features are a Dorman-Prince predictor-corrector scheme, forward modelling of non-conservative forces such as solar radiation pressure and atmospheric drag as well as antenna phase center corrections. EPOS-OC uses GPS zero-difference ionosphere-free code and phase data to estimate orbits and clocks of the GPS constellation and of the GRACE satellites, for details refer to Zhu *et al.* (2004).

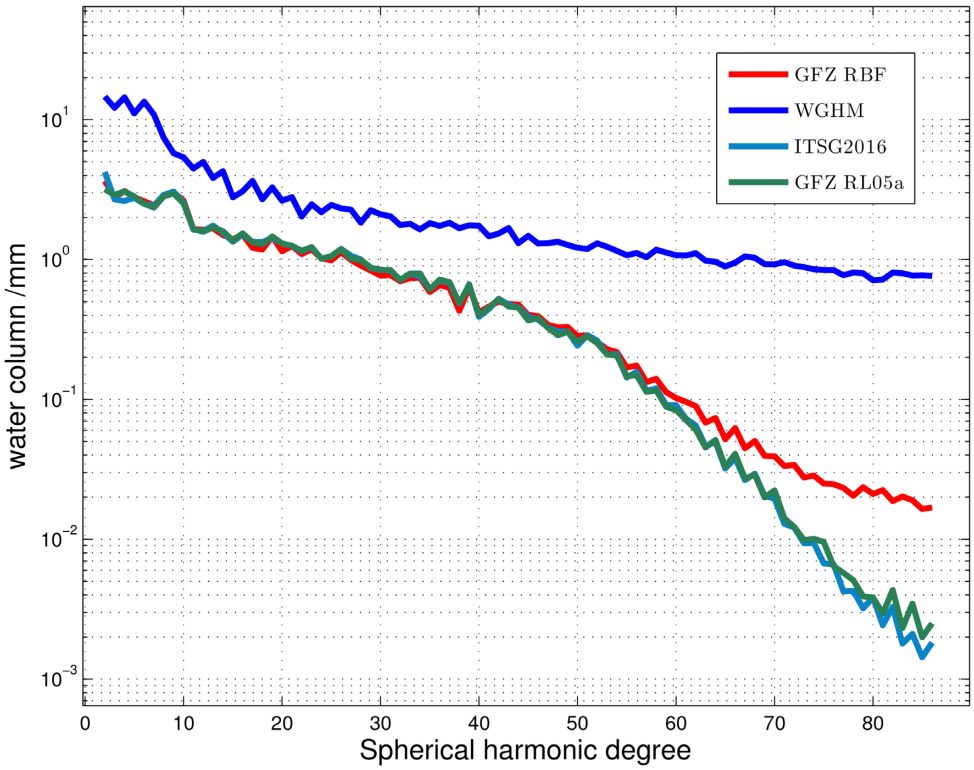

Figure 7. Spectral densities for the average time-variable GRACE signal, with linear trends being removed to compare to continental hydrology. Post-filtering with DDK4 (Kusche *et al.* 2009), applies to ITSG2016 and GFZ RL5a and corresponds to a low pass filtering with a pass band beginning at degree ≈50 resolution. The Kalman filtered RBFs maintain instead signal beyond degree 60 as no post-filtering is applied.

The orbital trajectories used in this study correspond to the trajectories that were computed for GFZ's latest GRACE RL05a. Data screening was performed semi-automatically, starting from a rapid science orbit without KBR use based on a gravity field model up to a high degree, including the time variable part from EIGEN-6C, Förste *et al.* (2011). The KBR residuals are screened, taking into account the GRACE Sequence Of Events (SOE) file. In case statistic thresholds are exceeded, data are excluded from further gravity field processing. The KBR weights relatively to the GPS code and phase observations are then iteratively increased in order to constrain the reduced dynamic orbit towards them.

The background forces, computed from the models listed in Table 1, have been subtracted in the domain of gradient differences from the GRACE observations prior to further data processing in the Kalman filter. Additionally, the CSR monthly C_{20} harmonic coefficients, Cheng *et al.* (2011), were applied to complement the derived gravity field solutions and to enable intercomparison.

7 SPECTRAL COMPARISONS

In this section, we compare SLR solutions to the time evolution of four geodetic parameters (Earth tesseral coefficients ΔC_{21}, ΔS_{21} and sectorial coefficients ΔC_{22}, ΔS_{22}) that are derived from the surface layer grids. These coefficients are of great importance because they are closely related to Earth's ellipsoid of inertia and sensitive to global water mass transfers, for example Cazenave *et al.* (1999). Chen *et al.* (2005) showed that the substitution of Earth orientation parameters (EOP) and SLR estimates for ΔC_{21}, ΔS_{21} and ΔC_{20} strongly affect the estimates of basin-scale water storage changes using GRACE time-variable gravity observations.

The coefficient estimates are obtained from the analysis of SLR observations to five geodetic satellites: LAGEOS-1 and 2, Starlette, Stella and Ajisai (*cf.* Cheng *et al.* 2011). The SLR analysis used for all of the degree-2 terms is consistent with the GRACE Release 05 processing, including the use of the identical Atmosphere-Ocean dealiasing model. The zonal harmonic series, C_{20}, was excluded as the GRACE twins are not very sensitive to them.

Fig. 5 displays time-series for each of these coefficients showing the agreement between the different solutions compared to the SLR results. We found all four coefficients in high similarity with the SLR derived series, considered as 'true' values, confirming the stability of the RBF method.

Fig. 6 shows a set of estimated amplitudes, $\sqrt{(C_{nm}^2 + S_{nm}^2)}$ after transformation of the time-variable grids into spherical harmonic coefficients, which (A) change from day-to-day, (B) the Kalman state as integrated value over past days, and last, (C) after the readdition of the mean model. Obviously, the measurement update of 1 d can address low spherical harmonic orders only, within the range defined by the longitude separation of the ground tracks. Driven by the least-squares prediction in the process model, the Kalman state subsequently accumulates more frequencies and the background restore finally completes the full time-variable signal.

The time-averaged degree variances in Fig. 7, are obtained from the spherical harmonic coefficients of the time-variable GRACE fields, and were computed from *ca*. 170 monthly fields and roughly 6000 daily grids.

The GFZ RBF solutions perform coherently, that is differences with respect to the mean time-variable GRACE signal content are comparable in amplitude and resolution. One has to keep in mind that the RBF's use a completely different approach from data preprocessing and integration until aspects of regularization. It is seen

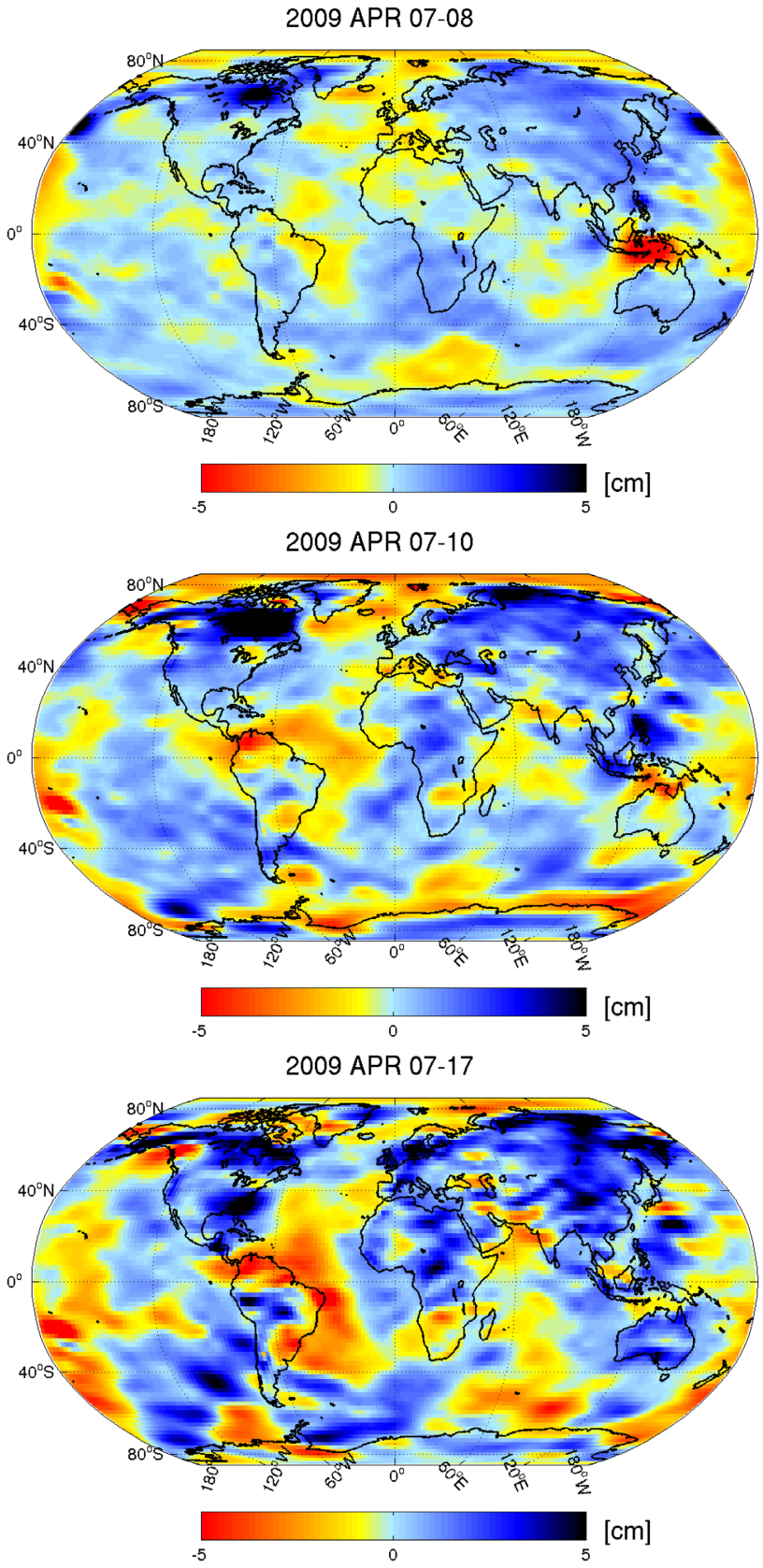

Figure 8. Short latency monitoring of changes over time. Top to bottom: 1-, 3- and 10-d changes of total water storage between daily solutions.

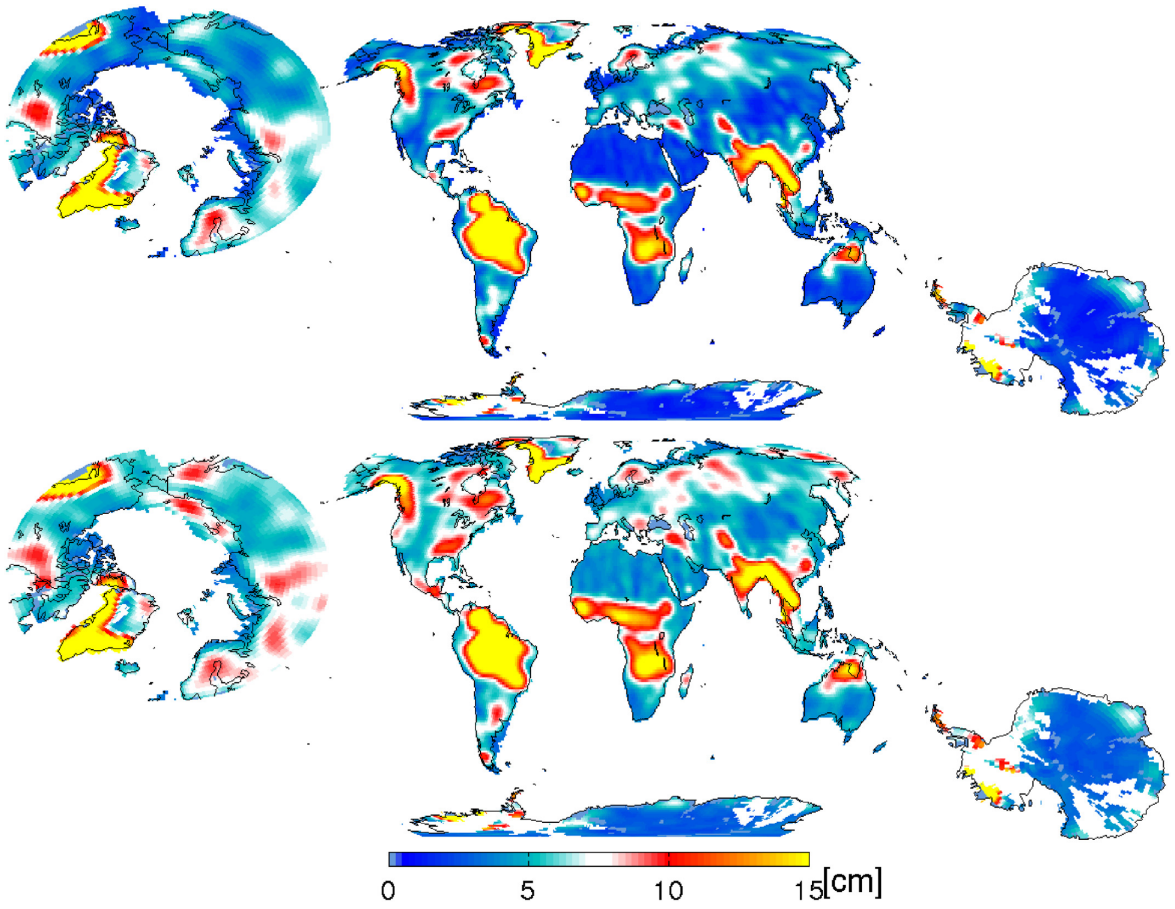

Figure 9. Global RMS variations of time variable mass transport captured by GRACE. Upper: daily Kalman solutions (GFZ RBF), lower: standard monthly GFZ RL05a products.

that the averaged daily solutions maintain signal power at higher frequencies, whereas the other solutions decrease due to the applied post-filtering after spherical harmonic degree 50.

8 SHORT LATENCY MONITORING

The aforementioned changes in the ground track pattern for subsequent months, amplified by an instable (unconstrained) data inversion and subsequent post-filtering, systematically affect the coefficient estimates and give results that poorly compare from one month to the next. For the regularized case, these problems disappear to a large extent, but at the expense of, for example proper trend estimates.

The Kalman filter approach combines the best of both worlds as follows: since the background model is based on unconstrained results, the short-term disturbing effects are averaged over longer time spans, thus leaving estimates unbiased. At the same time, the conditioning is preserved in the Kalman process model, enabling thus robust change detection over short time spans because the results become highly intercomparable. This gives a resilient opportunity for monitoring purposes. Fig. 8 shows the spatial patterns for the 1-, 3- and 10-d differences, exemplarily. We observe increasing signal over time for the continental and the near-polar regions (caused e.g. by the southern arctic circumpolar current). Continental hydrology signals are well captured, while striping and artefacts mainly over the oceans are suppressed.

Fig. 9 compares the signal RMS for the temporal-varying GRACE results over the complete mission period. Arid regions of low hydrological signal become clearly visible despite the fact that our process dynamic is widely isotropic throughout the surface grid.

Fig. 10 shows the RMS of the global differences between three reference solutions (ITSG 2016, CSR RL5 and GFZ RL05a) each of them computed from unregularized, post-filtered (DDK4) spherical harmonic coefficients and monthly averages of the daily RBF solutions. The monthly averaged RBF solutions correspond very well with the references. Main differences occur where strong continental hydrology is present. The GFZ RL05a solutions show systematic features that are not present in other solutions.

For further verification, we compared mass changes from GRACE with hydraulic simulations of the large scale annual inundation volume in the Mekong basin and delta (Fig. 11). A total of 12 gauging stations in Cambodia and Vietnam were used to calibrate simulated inundation volumes during the flood seasons (July–December) of 2008 to 2011 (Dung *et al.* (2011)). The strong correlation instills confidence in the GRACE derived high spatial and temporal resolution. Fig. 11 shows the daily GRACE Kalman solutions reflecting flood volume evolution very well and on shorter timescales than monthly averaged solutions. The dominant seasonal signal, which varies from year-to-year, however, is not fully captured, for example in 2010 (low) and 2011 (high). This may be attributed to the seasonal background modelling which is averaged

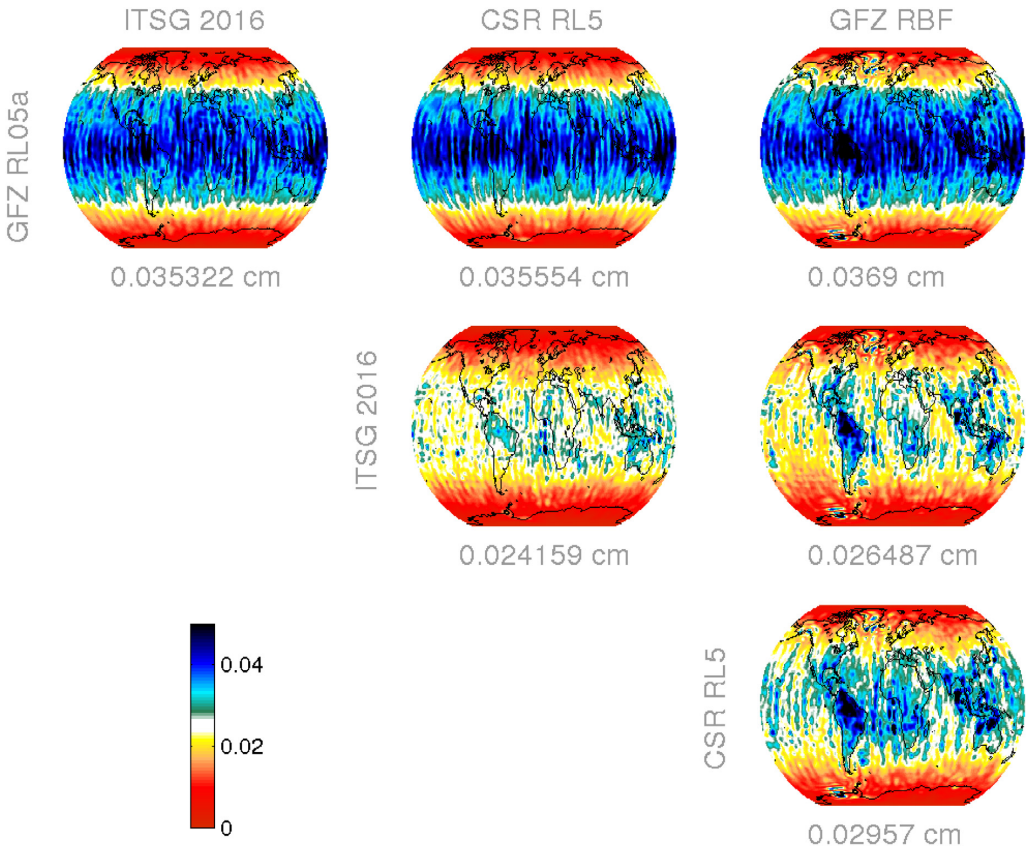

Figure 10. Intercomparison of the RMS differences for monthly averaged RBF solutions with other GRACE solutions. The comparison contains full time variable signal in equivalent water heights. While the global RMS comparisons reveals high correspondence of below 3 cm, some differences in continental hydrology are observed.

over the GRACE mission period and may need further refinement in future reprocessing efforts.

9 SUMMARY, CONCLUSIONS AND DISCUSSION

The NASA/German satellite mission GRACE, from 2002 to 2017 has had a great impact on mass transport and mass distribution modelling in the Earth's system. 15 yr of data and substantial improvements in the knowledge of the non-steric ocean topography and atmospheric pressure variations, now enables the evaluation of the total annual and semi-annual hydrological cycle, which can be evaluated in high spatial and temporal resolution.

Imposing statistical constraints from signal covariance modelling enables an increase in temporal resolution. Additionally, evaluation in the spatial domain enables us to impose geographic constraints, such as a land/ocean decoupling without deeper knowledge of signal characteristics.

In all, day-to-day impact from the derived GRACE observation data can be successfully modelled and evaluated. This is an important step towards near real-time monitoring of mass distribution processes inside the Earth and on the Earth's surface which is expected to improve global mass transfer estimates for climate monitoring and predictions. Further evaluation and comparison of results with other GRACE solutions can be found in an adjacent document (Gruber *et al.* 2018). In Gouweleeuw *et al.* (2018) a study on major flood events in the Ganges–Brahmaputra Delta from daily gravity solutions is discussed.

GRACE derived total water storage change is a horizontally and vertically integrated quantity and, as such, presents an opportunity for water balance studies. Differentiation between the different storage components, however, is not possible. For best closure, *in situ* hydrological data remain critical. Nevertheless, GRACE provides a big picture for the analysis and monitoring of hydrologic dynamics in, but not restricted to, the world's most poorly gauged river basins. Some key-features of the method presented are summarized below:

(i) robust against poor ground track patterns from commensurate orbital revolution period and Earth' rotation (repeat cycle orbit),
(ii) enhanced temporal resolution,
(iii) flexible towards regional solutions and refinements where enhanced local covariance information available,
(iv) no post filtering required (user-friendly),
(v) direct spatial constraining (e.g. land/ocean decoupling),
(vi) multi-mission combination with other space gravimetric techniques (e.g. SLR orbitography, gradiometry and sea surface topography from altimetry), since decorrelated *in situ* observations are available as by-product of the Kalman filter,
(vii) linear equations and low computational costs,
(viii) very short lead-time for data retrieval and inversion,
(ix) reduced artefacts from spatial localization compared to spherical harmonic coefficient estimation.

The method presented here is particularly useful in perspective of NASA/ GFZ's GRACE Follow-On mission where for the

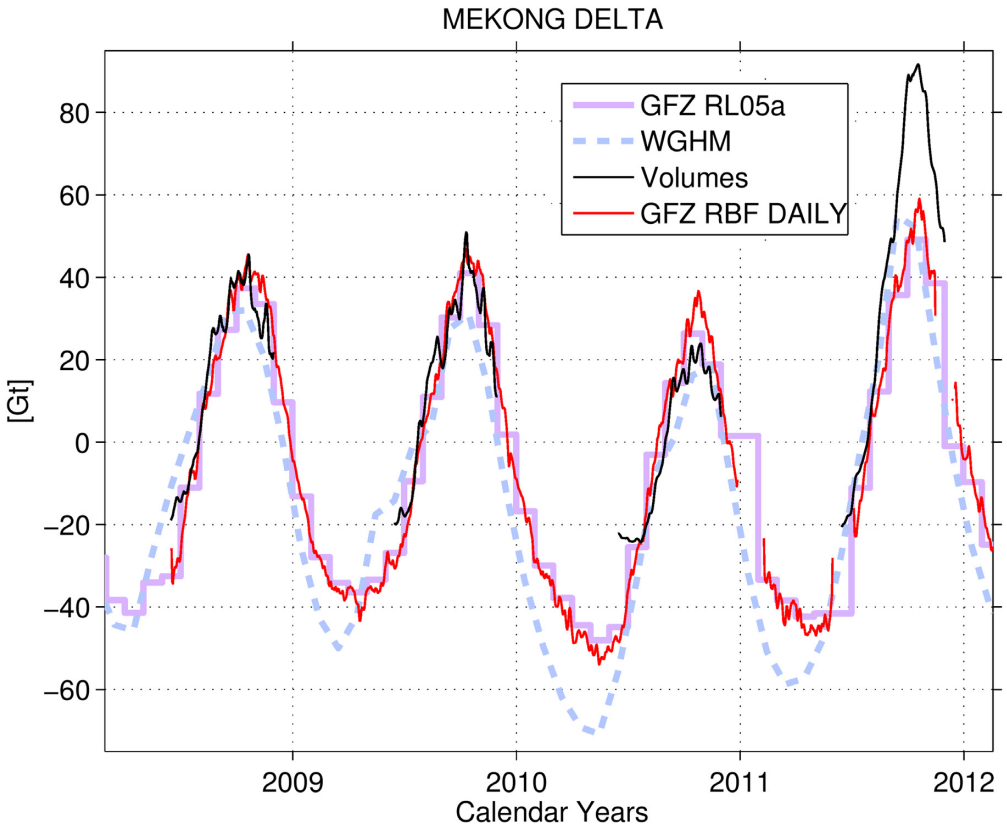

Figure 11. Monthly and daily GFZ derived solutions (stairs and red curve) compared to the respective inundation volumes in the lower Mekong river delta (black curve) and WGHM (light blue).

first time, an intersatellite laser link will be established in orbit. The introduction of then nanometer-accuracy measurements into the Kalman filter will take full advantage of advanced signal fusion.

Latest daily [2° × 2°] grids in equivalent water layer thickness, and [1° × 1°] grids with GIA predictions removed and center of mass to center of figure corrected, as well as dimensionless spherical harmonic coefficients, can be downloaded from ftp://gfzop.gfz-potsdam.de/EGSIEM/.

ACKNOWLEDGEMENTS

The authors would like to thank the German Space Operations Center (GSOC) of the German Aerospace Center (DLR) for providing continuous and nearly 100 per cent of the raw telemetry data of the twin GRACE satellites. The WGHM hydrological data sets are greatly appreciated. We would also like to thank the GFZ Science Data System for providing GRACE orbits and preprocessed KBR observation data.

This research was co-funded by the European Union's Horizon 2020 project European Gravity Service for Improved Emergency Management (EGSIEM) under the grant agreement No 637010. The article reflects only the authors' views. The Research Executive Agency is not responsible for any use that may be made of the information it contains.

We are gratefull to three reviewers who have helped to improve the manuscript. One of them, is particularly thanked for his high commitment and very constructive and productive comments that have improved the manuscript substantially.

REFERENCES

Bierman, G.J., 1977. *Factorization Methods for Discrete Sequential Estimation,* Dover Publications.

Castle, S.L., Thomas, B.F., Reager, J.T., Rodell, M., Swenson, S.C. & Famiglietti, J.S., 2014. Groundwater depletion during drought threatens future water security of the colorado river basin, *Geophys. Res. Lett,* **41,** 16, doi:10.1002/2014GL061055.

Cazenave, A., Mercier, F., Bouille, F. & Lemoine, J.-M., 1999. Global-scale interactions between the solid Earth and its fluid envelopes at the seasonal time scale, *Earth planet. Sci. Lett.,* **171,** 549–559.

Chen, J.L., Rodell, M., Wilson, C.R. & Famiglietti, J.S., 2005. Low degree spherical harmonic influences on gravity recovery and climate experiment (GRACE) water storage estimates, *Geophys. Res. Lett.,* **32,** doi:10.1029/2005GL022964.

Chen, Q., Shen, Y., Chen, W., Zhang, X., Hsu, H. & Ju, X., 2015. A modified acceleration-based monthly gravity field solution from GRACE data, *Geophys. J. Int.,* **202**(2), 1190–1206.

Cheng, M.K., Ries, J.C. & Tapley, B.D., 2011. Variations of the Earth's figure axis from satellite laser ranging and GRACE, *J. geophys. Res.,* **116,** B01409, doi:10.1029/2010JB000850.

Dahle, C., Flechtner, F., Gruber, C., König, D., König, R., Michalak, G. & Neumayer, K.-H., 2012. GFZ GRACE Level-2 Processing Standards Document for Level-2 Product Release 0005, Scientific Technical Report STR12/02 - Data, Revised Edition, January 2013, Potsdam, p. 21, doi:10.2312/GFZ.b103-1202-25.

Dobslaw, H., Flechtner, F., Bergmann-Wolf, I., Dahle, C., Dill, R., Esselborn, S., Sasgen, I. & Thomas, M., 2013. Simulating high-frequency atmosphere-ocean mass variability for de-aliasing of satellite gravity observations: AOD1B RL05, *J. geophys. Res.,* **118**(7), 3704–3711.

Döll, P., Kaspar, F. & Lehner, B., 2003. A global hydrological model for deriving water availability indicators: model tuning and validation, *J. Hydrol.,* **270,** 105–134.

Dung, N., Merz, B., Bárdossy, A., Thang, T. & Apel, H., 2011. Multi-objective automatic calibration of hydrodynamic models utilizing inundation maps and gauge data, *Hydrol. Earth Syst. Sci.,* **15**(4), doi:10.5194/hess-15-1339-2011.

Famiglietti, J.S. *et al.*, 2011. Satellites measure recent rates of groundwater depletion in California's central valley, *Geophys. Res. Lett.,* **38**(3), doi:10.1029/2010GL046442.

Farrell, W., 1972. Deformation of the Earth by surface loads, *Rev. Geophys. Space Phys.,* **10**(3), 761–797.

Förste, C. *et al.*, 2011. EIGEN-6: a new combined global gravity field model including GOCE data from the collaboration of GFZ-Potsdam and GRGS-Toulouse, in *Proceedings of the EGU General Assembly,* Vol. **13,** EGU2011-3242-2.

Gouweleeuw, B.T., Kvas, A., Gruber, C., Gain, A.K., Mayer-Gürr, T., Flechtner, F. & Güntner, A., 2018. Daily GRACE gravity field solutions track major flood events in the Ganges-Brahmaputra Delta, *Hydrol. Earth Syst. Sci.,* **22,** 2867–2880.

Gruber, C., Moon, Y., Flechtner, F., Dahle, C., Novák, P., König, R. & Neumayer, K.-H., 2013. Submonthly GRACE solutions from localizing integral equations and Kalman filtering, in *International Association of Geodesy Symposia, IAG Symp. 139, Earth on the Edge: Science for a Sustainable Planet,* eds Rizos, Chris & Willis, Pasca, Springer, ISBN 978-3-642-37221-62012.

Gruber, C., Rudenko, S., Groh, A., Ampatzidis, D. & Fagiolini, E., 2018. Earth's surface mass transport derived from GRACE, evaluated by GPS, ICESat, hydrological modeling and altimetry satellite orbits, *Earth Surf. Dyn.,* **6**(4), 1203–1218.

Güntner, A., Schmidt, R. & Döll, P., 2006. Supporting large-scale hydrological monitoring and modelling by time-variable gravity data, *Hydrogeol. J.,* **15**(1), 167–170.

Heiskanen, W.A. & Moritz, H., 1967. *Physical & Geodesy,* W.H. Freeman Company.

Hobson, W.E., 1955. *The Theory of Spherical and Ellipsoidal harmonics,* Chelsea Publishing Company.

Klees, R., Revtova, E.A., Gunter, B.C., Ditmar, P., Oudman, E., Winsemius, H.C. & Savenije, H.H.G., 2008. The design of an optimal filter for monthly grace gravity models, *Geophys. J. Int.,* **175,** 417–432.

Koop, R. & Stelpstra, D., 1989. On the computation of the gravitational potential and its first and second order derivatives, *Manuscr. Geod., Springer Verlag,* **14,** 373–382.

Krarup, T., 2006. *Mathematical Foundation of Geodesy, Selected papers of Thorben Krarup,* ed. Borre, K., Springer Verlag, ISBN: 3-540-33765-2.

Kurtenbach, E., Mayer-Gürr, T. & Eicker, A., 2009. Deriving daily snapshots of the Earth's gravity field from GRACE L1b data using Kalman filtering, *Geophys. Res. Lett.,* **36**(17), doi:10.1029/2009GL039564 .

Kurtenbach, E., Eicker, A., Mayer-Gürr, T., Holschneider, M., Hayn, M., Fuhrmann, M. & Kusche, J., 2012. Improved daily gravity field solutions using a Kalman smoother, *J. Geodyn.,* **59-60,** 39–48.

Kusche, J., Schmidt, R., Petrović, S. & Rietbroek, R., 2009. Decorrelated GRACE time-variable gravity solutions by GFZ, and their validation using a hydrological model, *J. Geod.,* **83,** 903–913.

Kvas, A., Gouweleeuw, B.T., Mayer-Gürr, T. & Güntner, A., 2016. Near real-time GRACE gravity field solutions for hydrological monitoring applications, in *Proceedings of the EGU General Assembly,* Vienna, Austria.

Landau, H., 1985. *Fourier Techniques and Applications,* Springer.

Lemoine, J.-M., Bruinsma, S., Gégout, P., Biancale, R. & Bourgogne, S., 2013. Release 3 of the GRACE gravity solutions from CNES/GRGS, Vol. **15**.

Moritz, H., 1980. *Advanced Physical Geodesy,* Wichmann Bd. 13.

Novák, P., 2007. Integral inversion of SST data of type GRACE, *Stud. Geophys. Geod.,* **51,** 351–367.

Petit G. &Luzum B., 2010. IERS conventions (2010), (Technical Note ; 36), Verlag des Bundesamts für Kartographie und Geodäsie, Frankfurt am Main, pp. 179, ISBN 3–89888–989–6.

Petrovello, M., 2013. GNSS filtering options, *Inside GNSS.*

Rowlands, D.D., Luthke, S.B., McCarthy, J.J., Klosko, S.M., Chinn, D.S., Lemoine, F.G., Boy, J.P. & Sabaka, T.J., 2010. Global mass flux solutions from GRACE: a comparison of parameter estimation strategies: mass concentrations versus stokes coefficients, *J. geophys. Res.,* **107,** B01403.

Rummel, R., 1979. Determination of short-wavelength components of the gravity field from satellite-to-satellite tracking or satellite gradiometry an attempt to an identification of problem areas, *Man. Geodyn.,* **4**(2), 107–148.

Savcenko, R. & Bosch, W., 2011. EOT11a—a new tide model from multi-mission altimetry, in *Proceedings of the OSTST Meeting,* San Diego, 19–21 October 2011.

Schmeer, M., Schmidt, M., Bosch, W. & Seitz, F., 2012. Separation of mass signal within GRACE monthly gravity field models by means of empirical orthogonal functions, *J. Geodyn.,* **59-60,** 124–132.

Schneider, F., 1997, Inverse problems in satellite geodesy and their approximate solution by splines and wavelets, *Diss*., Universität Kaiserslautern, Shaker Verlag, Aachen.

Shabanloui, A. & Müller, J., 2015. Mass variations in the siberian permafrost region based on new GRACE results and auxiliary modeling, in *IGFS 2014,* eds Jin, S. & Barzaghi, R., International Association of Geodesy Symposia.

Swenson, S. & Wahr, J., 2006. Post-processing removal of correlated errors in GRACE data, *Geophys. Res. Lett.,* **33**(8), L08402, doi:10.1029/2005GL025285.

Tangdamrongsub, N., Hwang, C.H., Shum, C.K. & Wang, L., 2012. Regional surface mass anomalies from GRACE KBR measurements: application of L-curve regularization and a-priori hydrological knowledge, *J. geophys. Res.,* **117,** B11406.

Tapley, B., Bettadpur, S. & Watkins, M., 2004. The gravity recovery and climate experiment: mission overview and early results., *Geophys. Res. Lett.,* **31,** L09607.

Van Camp, M., De Viron, V., Métivier, L., Meurers, B. & Francis, O., 2013. The quest for a consistent signal in ground and GRACE gravity time-series, *Geophys. J. Int.,* **197,** 192–201.

Wahr, J., Molenaar, M. & Bryan, F., 1998. Time variability of the Earth's gravity field: hydrological and oceanic effects and their possible detection using GRACE, *J. geophys. Res.,* **103**(12), 30 205–30 229.

Weigelt, M., 2017. The acceleration approach, in *Global Gravity Field Modeling from Satellite-to-Satellite Tracking Data. Lecture Notes in Earth System Sciences,* eds Naeimi, M. & Flury, J., Springer, doi:10.1007/978-3-319-49941-3.

Zhang, Z., Chao, B., Lu, Y. & Hsu, H., 2009. An effective filtering for GRACE time-variable gravity: fan filter, *Geophys. Res. Lett.,* **36**(17), L17311, doi:10.1029/2009GL039459.

Zhu, S., Reigber, C. & König, R., 2004. Integrated adjustment of CHAMP, GRACE, and GPS data, *J. Geod.,* **78**(1-2), 103–108.

APPENDIX A: POISSON KERNEL

The Newtonian potential of a surface layer on the sphere to an arbitrary point in external space is given by

$$V(\mathbf{x}) = \frac{\mathrm{G}}{4\pi}\,\mathrm{R}^2 \int_{\omega}\int_{\mathrm{R}}^{\mathrm{R}'} \frac{\rho_r}{l}\,\mathrm{d}r\,\mathrm{d}\omega\,, \qquad \mathrm{d}\omega = \sin\theta\,\mathrm{d}\theta\,\mathrm{d}\lambda\,, \tag{A1}$$

where G is the universal gravitational constant, R is the radius of the reference sphere, R'–R is the layer thickness, ρ_r is the specific (constant) density of the volume element on the sphere and θ and λ are the geocentric colatitude and longitude. For the external point holds, $\mathbf{x} = \{r, \theta, \lambda\}$. For the inverse distance (l) between surface points and exterior masses an infinite series of Legendre polynomials exist (e.g. Heiskanen & Moritz 1967),

$$l^{-1} = \frac{1}{\mathrm{R}} \sum_{n=0}^{\infty} \left(\frac{\mathrm{R}}{r}\right)^{n+1} P_n(\cos\psi), \qquad r > \mathrm{R}. \tag{A2}$$

where ψ is the spherical distance between external and surface points, $\psi\angle(\mathbf{x}, \mathbf{y})$. Evaluating differential mass-elements on the surface of the reference sphere to

$$\mathrm{d}m = \rho_r \mathrm{R}^2 h \mathrm{d}\omega, \quad \text{with} \quad h = \int_{\mathrm{R}}^{\mathrm{R}'} \mathrm{d}r\,, \tag{A3}$$

and combining the previous three equations leads to

$$V(\mathbf{x}) = \frac{\mathrm{G}}{4\pi} \int_{\omega} \frac{\mathrm{d}m}{\mathrm{R}} \left[\sum_{n=0}^{\infty} (2n+1) \left(\frac{\mathrm{R}}{r} \right)^{n+1} P_n(\cos\psi) \right], \tag{A4}$$

with a factor $(2n + 1)$ that compensates the metric of the Legendre Polynomials

$$\int_{\omega} [P_n(\cos\psi)]^2 \,\mathrm{d}\omega = \frac{4\pi}{2n+1}\,. \tag{A5}$$

Evaluation of the brackets in eq. (A4) yields Poisson's kernel (*cf.* Heiskanen & Moritz 1967)

$$\frac{\mathrm{R}(r^2 - \mathrm{R}^2)}{l^3} = \sum_{n=0}^{\infty} (2n+1) \left(\frac{\mathrm{R}}{r} \right)^{n+1} P_n(\cos\psi), \tag{A6}$$

providing a rigorous means for the evaluation of time variable mass transport on the sphere.

APPENDIX B: GRACE INTEGRAL KERNEL

Referring to Earth' surface ω_e, approximated by the bounding sphere (assuming that all relevant gravitational masses are entirely embedded inside the surface) of radius R we can follow the theory of surface integrals with evaluation points $(\mathbf{x})$ and gridpoints $(\mathbf{y})$ over the surface element $d\omega$

$$V(\mathbf{x}) = \frac{1}{4\pi} \int_{\omega} V(\mathbf{y})\, \mathcal{K}(\mathbf{x}, \mathbf{y})\, \mathrm{d}\omega, \qquad |\mathbf{x}| \geqslant |\mathbf{y}| \tag{B1}$$

mapping quantities, for example from a regular grid to evaluation points. The reproducing kernel according to eq. (A4) for this operation reads

$$\mathcal{K}(\mathbf{x}, \mathbf{y}) = \sum_{n} (2n+1) \left(\frac{R}{r} \right)^{n+1} P_n(\cos\psi) \tag{B2}$$

with the Legendre polynomial per degree, P_n and the spherical distance ψ between evaluation and gridpoints. For the GRACE-*SST* observation type the observations are considered as functions of the geo-potential (*cf.* Novák 2007)

$$f[V(\mathbf{x})] = \langle \delta\nabla_x V, \delta\mathbf{x} \rangle\,, \tag{B3}$$

where gradient differences of the gravitational potential between the twin-satellites, $\delta\nabla_x V$ are projected onto the intersatellite direction and scaled by the distance between them, $\delta x = |\mathbf{x_2} - \mathbf{x_1}|$. The notation $\langle \cdot, \cdot \rangle$, denotes the scalar vector product. Applying the operator $\delta\nabla_x$ to Poisson's Kernel, eq. (B2), the resulting scalar integral function takes the form

$$\mathcal{H}(\mathbf{x_1}, \mathbf{x_2}, \mathbf{y}) = \langle \delta\nabla_x \mathcal{K}(\mathbf{x}, \mathbf{y}), \delta\mathbf{x} \rangle\,. \tag{B4}$$

with the expansion

$$\delta\nabla_x \mathcal{K}(\mathbf{x}, \mathbf{y}) = \nabla_x \mathcal{K}(\mathbf{x_2}, \mathbf{y}) - \nabla_x \mathcal{K}(\mathbf{x_1}, \mathbf{y})\,. \tag{B5}$$

The gradient difference in line-of-sight from eq. (B3) can serve as a *proxy-observables* for the orbital and K-band ranging data,

$$\ell = ||\delta\mathbf{v}||^2 - \dot{\rho}^2 - \rho\ddot{\rho} = \langle \delta\nabla_x V, \delta\mathbf{x} \rangle\,, \tag{B6}$$

where $||\delta\mathbf{v}||$ is the intersatellite velocity and ρ, $\dot{\rho}$ and $\ddot{\rho}$ are range, range–rate and range–acceleration observables, respectively.

Eq. (B6) can be rewritten to

$$\left\langle \delta\nabla_x V, \mathbf{e}^{\mathrm{LOS}} \right\rangle \cdot \rho = \langle \delta\mathbf{v}, \delta\mathbf{v} \rangle - \left\langle \delta\mathbf{v}, \mathbf{e}^{\mathrm{LOS}} \right\rangle^2 - \rho\ddot{\rho}, \tag{B7}$$

$$\left\langle \delta\nabla_x V, \mathbf{e}^{\mathrm{LOS}} \right\rangle = \left\langle \delta\mathbf{v}, \mathbf{e}^{\perp} \right\rangle^2 / \rho - \ddot{\rho}, \tag{B8}$$

where $\mathbf{e}^{\mathrm{LOS}}$ denotes the direction in line-of-sight and $\mathbf{e}^{\perp}$ is in the perpendicular plane to it,

$$\left\langle \mathbf{e}^{\mathrm{LOS}}, \mathbf{e}^{\perp} \right\rangle = 0. \tag{B9}$$

The relation between range-accelerations and gradient differences thus becomes obvious in eq. (B8) that is completed by perpendicular, that is mainly radial forcing. Eq. (B1) becomes

$$\ell = \frac{1}{4\pi} \int_{\omega} V(\mathbf{y})\, \mathcal{H}(\mathbf{x_1}, \mathbf{x_2}, \mathbf{y})\, \mathrm{d}\omega. \tag{B10}$$

where the Kernel $\mathcal{H}$ is obtained rigorously from the gradient differences

$$\mathcal{H} = \rho \cdot \delta\{[\mathcal{K}_r\ \mathcal{K}_\theta\ \mathcal{K}_\lambda] \cdot [\mathbf{e}_r\ \mathbf{e}_\theta\ \mathbf{e}_\lambda]^T\} \tag{B11}$$

with the partial derivatives for the gradient of $\mathcal{K}$ in geocentric spherical coordinates (r, θ, λ)

$$\mathcal{K}_r = -\frac{1}{R} \sum_{n} (2n+1)(n+1) \left(\frac{R}{r} \right)^{n+2} P_n(\cos\psi) \tag{B12}$$

$$\mathcal{K}_\Theta = +\frac{1}{R} \sum_{n} (2n+1) \left(\frac{R}{r} \right)^{n+2} \mathrm{D}_\psi P_n(\cos\psi) \cos\alpha \tag{B13}$$

$$\mathcal{K}_\lambda = -\frac{1}{R} \sum_{n} (2n+1) \left(\frac{R}{r} \right)^{n+2} \mathrm{D}_\psi P_n(\cos\psi) \sin\alpha \tag{B14}$$

with the differentiation operator D_ψ w.r.t. to the spherical distance and the local spherical basis

$$\mathbf{e}_r = [\sin\theta\cos\lambda,\ \sin\theta\sin\lambda,\ \cos\theta] \tag{B15}$$

$$\mathbf{e}_\theta = [\cos\theta\cos\lambda,\ \cos\theta\sin\lambda,\ -\sin\theta] \tag{B16}$$

$$\mathbf{e}_\lambda = [-\sin\lambda,\ \cos\lambda,\ 0]\,. \tag{B17}$$

The derivatives of the Legendre Polynomials, eqs (B13) and (B14) can be found (e.g. Koop & Stelpstra 1989). The spherical distance $\psi\measuredangle(\mathbf{x}, \mathbf{y})$ between evaluation and surface gridpoints can be evaluated by the law of cosines

$$\cos\psi = \cos\theta\cos\theta_g + \sin\theta \cdot \sin\theta_g \cdot \cos(\lambda - \lambda_g) \tag{B18}$$

and the respective azimuth angle α reads

$$\tan\alpha = \frac{\sin\theta_g \cdot \sin(\lambda - \lambda_g)}{\sin\theta \cdot \cos\theta_g - \cos\theta \cdot \sin\theta_g \cdot \cos(\lambda - \lambda_g)}. \tag{B19}$$